

FUNDAMENTALS & APPLICATIONS

CHEMELECTROCHEM

ANALYSIS & CATALYSIS, BIO & NANO, ENERGY & MORE

Accepted Article

Title: Enhanced cycling performance of magnesium doped lithium cobalt phosphate

Authors: EunJeong Kim, David Miller, John Irvine, and Anthony Robert Armstrong

This manuscript has been accepted after peer review and appears as an Accepted Article online prior to editing, proofing, and formal publication of the final Version of Record (VoR). This work is currently citable by using the Digital Object Identifier (DOI) given below. The VoR will be published online in Early View as soon as possible and may be different to this Accepted Article as a result of editing. Readers should obtain the VoR from the journal website shown below when it is published to ensure accuracy of information. The authors are responsible for the content of this Accepted Article.

To be cited as: *ChemElectroChem* 10.1002/celc.201901372

Link to VoR: <http://dx.doi.org/10.1002/celc.201901372>

WILEY-VCH

www.chemelectrochem.org

A Journal of



Enhanced cycling performance of magnesium doped lithium cobalt phosphate

Eun Jeong Kim,^[a,b] David N. Miller,^[a] John T.S. Irvine,^[a] and A. Robert Armstrong^{*[a,b]}

Abstract: The cycling performance of LiCoPO₄ (LCP) as a high voltage positive electrode material in lithium-ion batteries is enhanced by partial magnesium substitution for cobalt. Structural investigation of magnesium doped LCP using combined powder neutron and X-ray diffraction reveals a decrease in anti-site defects. In addition, the reduced unit cell volume variation during the charging process is observed by *operando* X-ray diffraction measurements. Characterisation of the surface shows the presence of a Mg-rich layer on the surface that might prevent detrimental reactions with the electrolyte. The combined beneficial effects of magnesium doping in LCP result in improved capacity retention.

Introduction

Lithium cobalt phosphate (LiCoPO₄) has been a strong candidate as a high voltage positive electrode material in lithium-ion batteries since first identified by Amine *et al.*^[1] However, unsatisfactory electrochemical performance associated with low electronic^[2-4] and ionic^[5] conductivities as well as significant capacity fade^[6,7] have been major obstacles to its wide application. Extensive studies have been devoted to mitigate these drawbacks including partial substitution of cobalt with transition or alkaline earth metals,^[3,8-16] surface modification^[17-23] and reduction of the particle size.^[24-27] The use of novel separators,^[28,29] functional electrolytes^[30-32] and polysaccharide-type binders^[33] have been also reported to improve the electrochemical performance of isostructural lithium iron phosphate (LiFePO₄) has improved via aliovalent or isovalent doping of either lithium sites or iron sites albeit the role of dopants has sometimes been controversial,^[34] partial substitution of transition metals for cobalt has been extensively investigated.^[3,9-12,35-42] However, very few studies have been reported on the electrochemically inactive dopant magnesium^[13-16] although its beneficial effects including structural stability during electrochemical cycling and modification of redox processes have been exploited in the phospho-olivine family.^[43-46] Here, we investigated the synthesis and characterisation of magnesium doped lithium cobalt phosphates, LiMg_xCo_{1-x}PO₄ ($x = 0, 0.05, 0.10, 0.15$ and 0.20). The effects of magnesium doping on various properties are investigated including morphology,

structure, electrochemical properties, surface and phase evolution during electrochemical cycling.

Results and Discussion

Characterisation of magnesium doped lithium cobalt phosphate materials

Fig. 1 shows the powder X-ray diffraction (PXRD) patterns of LiMg_xCo_{1-x}PO₄ ($x = 0, 0.05, 0.10, 0.15$ and 0.20) prepared by solvothermal synthesis. All diffraction peaks can be indexed on the basis of an orthorhombic olivine structure (space group *Pnma*). All samples are single-phase without any additional peaks except LiMg_{0.2}Co_{0.8}PO₄, which contains some diffraction peaks from an impurity phase, assigned to Li₃PO₄ (ICSD database no.77095). It has been reported that the formation of impurities depends on the concentration and pH of reagents in hydrothermal and solvothermal synthetic methods.^[47,48] In this study, additional MgSO₄ may influence the pH of reaction medium, resulting in the formation of impurity phase Li₃PO₄.

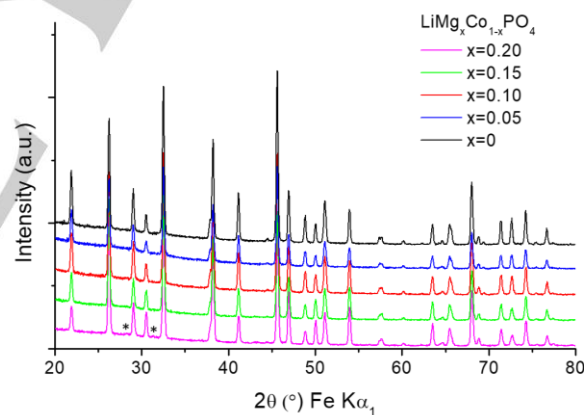


Fig. 1. PXRD patterns of as-synthesised LiMg_xCo_{1-x}PO₄, where $x=0$ (black), $x=0.05$ (blue), $x=0.10$ (red), $x=0.15$ (green) and $x=0.20$ (magenta) recorded with Fe K α_1 radiation. * represents impurity peaks from Li₃PO₄.

The refined unit cell parameters and profile fits using the Le Bail method are shown in Fig. 2 and Fig. S1. The cell parameter *a* decreases significantly with increased substitution of Mg. This confirms successful substitution of Mg for Co as the radius of Mg²⁺ (0.72 Å, six-fold coordination) is smaller than that of Co²⁺ (0.745 Å, six-fold coordination, high spin).

[a] E. J. Kim, Dr. D. Miller, Pr. J. T. S. Irvine and Dr. A. R. Armstrong,* School of Chemistry, University of St Andrews, St Andrews, Fife, KY16 9ST, United Kingdom. E-mail: ara@st-andrews.ac.uk

[b] E. J. Kim, Dr. A. R. Armstrong, ALISTORE-ERI, 80039, Amiens Cedex, France.

Supporting information for this article is given via a link at the end of the document.

ARTICLE

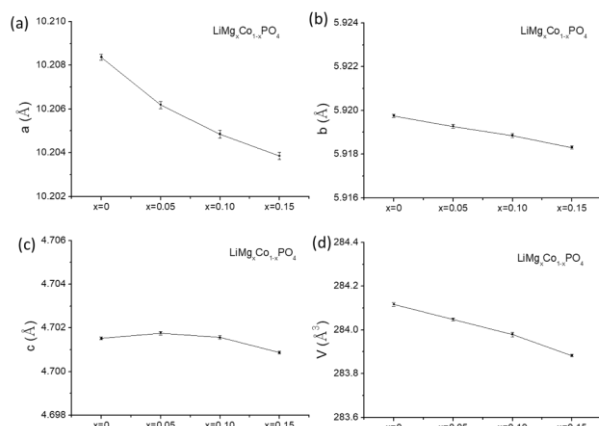


Fig. 2. Refined results using the Le Bail method (a) unit cell parameter a , (b) unit cell parameter b , (c) unit cell parameter c and (d) unit cell volume.

In order to obtain detailed crystallographic information, combined refinements were performed using PXRD and powder neutron diffraction (PND) data. As aliovalent doping on Li sites is shown to be energetically unfavourable,^[49] Mg doping on Co sites was solely considered. As shown in Table S1, Fig. S2 and S3, good fits were obtained with R_{wp} of less than 4 %, confirming the model is reliable. The compositions derived from the occupancy of combined refinements are in good agreement with the values deduced by inductively coupled plasma optical emission spectroscopy (ICP-OES) analysis except for $\text{LiMg}_{0.15}\text{Co}_{0.85}\text{PO}_4$ (Table 1). The difference might originate from a Mg-rich phase present around particle edges which is undetectable with diffraction methods but was observed in energy dispersive X-ray spectroscopy (EDS) mapping (Fig. 3.d). The transmission electron microscopy (TEM) image shows a well-crystallised compound as well as a Mg-rich layer and the contrast observed in scanning transmission electron microscope (STEM) agrees with the elemental (Co and Mg) distribution (Fig. 3). Of note, anti-site defects, involving partial exchange of Li and Co between 4a and 4c sites, diminish as more Mg is substituted for Co.

Table 1. Stoichiometric ratio derived from combined refinement and ICP-OES

Samples	Composition	
	Combined refinement	ICP-OES
$\text{LiMg}_x\text{Co}_{1-x}\text{PO}_4$		
$x = 0$	LiCoPO_4	
$x = 0.05$	$\text{LiMg}_{0.06}\text{Co}_{0.94}\text{PO}_4$	$\text{LiMg}_{0.04}\text{Co}_{0.96}\text{PO}_4$
$x = 0.10$	$\text{LiMg}_{0.08}\text{Co}_{0.92}\text{PO}_4$	$\text{LiMg}_{0.08}\text{Co}_{0.92}\text{PO}_4$
$x = 0.15$	$\text{LiMg}_{0.07}\text{Co}_{0.93}\text{PO}_4$	$\text{LiMg}_{0.12}\text{Co}_{0.88}\text{PO}_4$

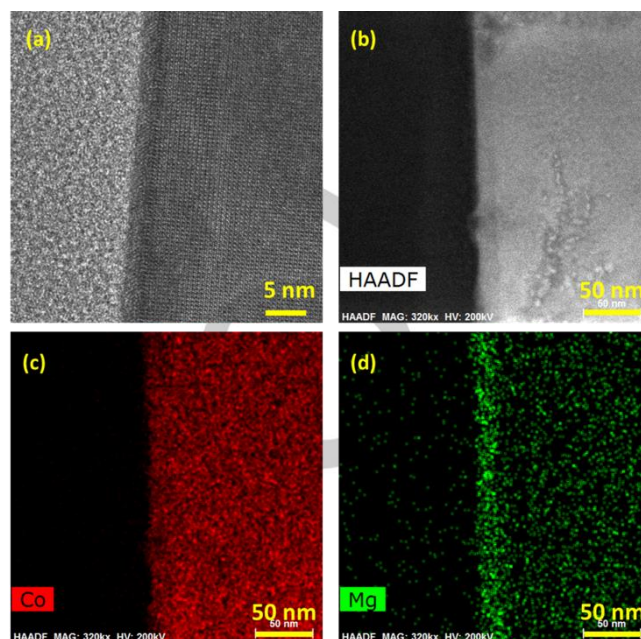


Fig. 3. (a) Bright-field TEM image, (b) High-angle annular dark-field STEM image and EDS mapping for (c) Co and (d) Mg elements of as-synthesised $\text{LiMg}_{0.15}\text{Co}_{0.85}\text{PO}_4$.

The EDS spectra of as-synthesised materials collected at 15 keV (Fig. 4) demonstrate a continuous increase of the proportion of Mg with decrease in Co content, consistent with the results from ICP-OES. All samples contain traces of sulphur which are probably related to by-products of sulphate anions from the precursors during solvothermal synthesis as previously reported.^[40,50]

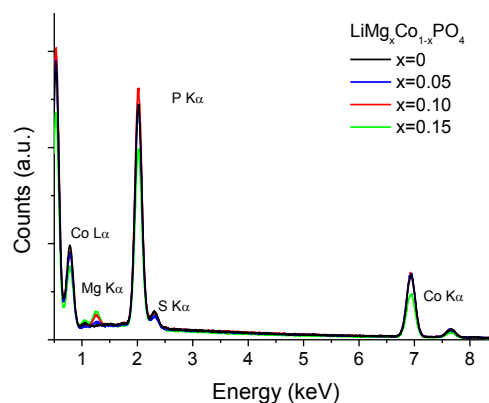


Fig. 4. EDS spectra of as-synthesised $\text{LiMg}_x\text{Co}_{1-x}\text{PO}_4$, where $x=0$ (black), $x=0.05$ (blue), $x=0.10$ (red) and $x=0.15$ (green).

The morphology of as-synthesised samples was investigated using scanning electron microscopy (SEM) (Fig. 5.a-d). LiCoPO_4 consists of sub-micron hexagonal platelets with the thickness of 100-150 nm, consistent with the reports that the ethylene glycol/water co-solvent system produces hexagonal platelets.^[51,52] The substitution of Mg for Co in LiCoPO_4 tends to

ARTICLE

enlarge particle size. Large particles emerge from $\text{LiMg}_{0.10}\text{Co}_{0.90}\text{PO}_4$ while $\text{LiMg}_{0.05}\text{Co}_{0.95}\text{PO}_4$ shows little change. A significant particle size difference is observed at $\text{LiMg}_{0.15}\text{Co}_{0.85}\text{PO}_4$ with the particle thickness about 1 μm . An analogous trend was reported in Fe-substituted LiCoPO_4 synthesised by a solvothermal method where a remarkable particle alteration to micrometer particles with a thickness above 500 nm was obtained, which is also observed under different synthesis conditions such as temperature and time.^[40] In this study, tentative syntheses reducing solvothermal treatment time from 16 h to 3 h ($\text{LiMg}_{0.15}\text{Co}_{0.85}\text{PO}_4$ - 3h) and temperature from 220 °C to 180 °C ($\text{LiMg}_{0.15}\text{Co}_{0.85}\text{PO}_4$ - 180°C) were carried out. As shown in Fig. 5.e, shorter reaction time barely affects the morphology. In contrast, lower temperature permits a reduction in the particle size but this leads to inhomogeneous size distribution (Fig. 5.f) and the appearance of an impurity phase (Fig. S4).

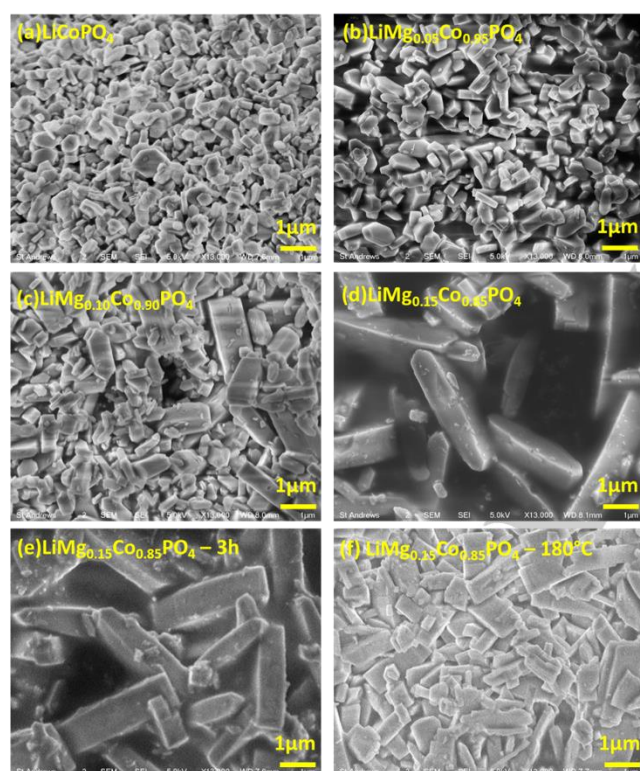


Fig. 5. SEM images of as-synthesised (a) LiCoPO_4 , (b) $\text{LiMg}_{0.05}\text{Co}_{0.95}\text{PO}_4$, (c) $\text{LiMg}_{0.10}\text{Co}_{0.90}\text{PO}_4$, (d) $\text{LiMg}_{0.15}\text{Co}_{0.85}\text{PO}_4$, (e) $\text{LiMg}_{0.15}\text{Co}_{0.85}\text{PO}_4$ - 3h and (f) $\text{LiMg}_{0.15}\text{Co}_{0.85}\text{PO}_4$ - 180 °C.

Electrochemical behaviour of magnesium doped lithium cobalt phosphate materials

In order to investigate Mg substitution effects on electrochemical performance, electrodes with a series of Mg-doped LiCoPO_4 were prepared then coin cells were tested at a rate of 16.7 mA g^{-1} (C/10 for LiCoPO_4). Fig. 6.a shows charge/discharge curves of LiCoPO_4 at cycle 1, 5, 10, 20 and 30. Typically two plateaus are present in the voltage profiles at all cycles, indicating two biphasic redox processes. It is known that the redox process of $\text{Co}^{2+}/\text{Co}^{3+}$ in LiCoPO_4 occurs through two schemes, with an intermediate phase of composition $\text{Li}_{2/3}\text{CoPO}_4$, coexisting with the fully lithiated

phase (LiCoPO_4) at higher Li content and with the fully delithiated phase at lower Li content.^[53-55] Both reversible processes are maintained for all Mg-substituted samples, producing two plateaus for all cycles (Fig. 6.b-d). On the first cycle, all samples show significant irreversible capacity with Coulombic efficiencies of 68 %, 63 %, 64 % and 57 % for LiCoPO_4 , $\text{LiMg}_{0.05}\text{Co}_{0.95}\text{PO}_4$, $\text{LiMg}_{0.10}\text{Co}_{0.90}\text{PO}_4$ and $\text{LiMg}_{0.15}\text{Co}_{0.85}\text{PO}_4$, respectively, due to electrolyte decomposition and/or possible SEI layer formation at high voltage. The efficiencies however increase, reaching about 92 % at the second cycle for all samples and around 98 % at cycle 30 (Fig. 6.e).

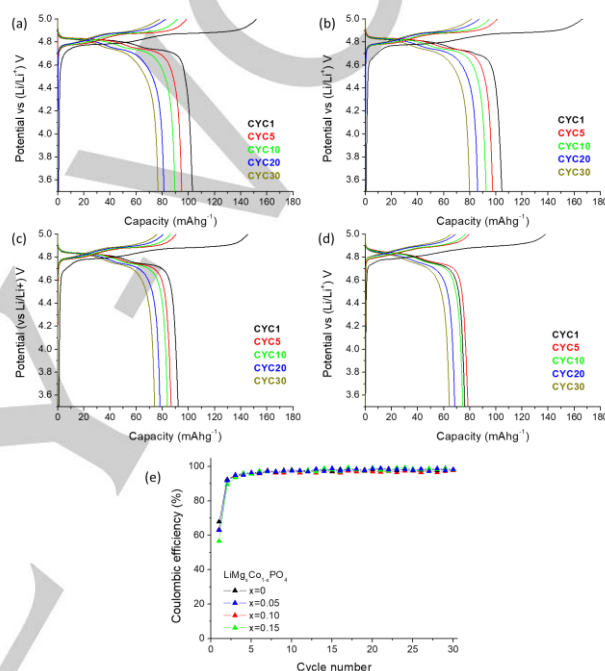


Fig. 6. Charge/discharge curves at cycle 1 (black), cycle 5 (red), cycle 10 (green), cycle 20 (blue) and cycle 30 (dark yellow) of (a) LiCoPO_4 , (b) $\text{LiMg}_{0.05}\text{Co}_{0.95}\text{PO}_4$, (c) $\text{LiMg}_{0.10}\text{Co}_{0.90}\text{PO}_4$, (d) $\text{LiMg}_{0.15}\text{Co}_{0.85}\text{PO}_4$ and (e) Coulombic efficiencies of LiCoPO_4 (black), $\text{LiMg}_{0.05}\text{Co}_{0.95}\text{PO}_4$ (blue), $\text{LiMg}_{0.10}\text{Co}_{0.90}\text{PO}_4$ (red) and $\text{LiMg}_{0.15}\text{Co}_{0.85}\text{PO}_4$ (green), cycled between 3.5 and 5.0 V vs Li/Li^+ at a rate of 16.7 mA g^{-1} .

Cycling performance of all samples is shown in Fig. 7.a. It is clearly observed that as more Mg is substituted for Co, a lower initial discharge capacity is delivered. This is attributed to the replacement of the electrochemically active Co^{2+} ions with electrochemically inactive Mg^{2+} ions.^[56] In addition to that, enlargement of the particle size might limit ionic transport, resulting in lower capacity. However, the capacity retention is improved as a function of Mg substitution as presented in Fig. 7.b. The normalised capacity retention based on the capacity delivered at the first cycle shows the highest capacity retention of 82 % for $\text{LiMg}_{0.15}\text{Co}_{0.85}\text{PO}_4$, followed by 80 %, 76 % and 74 % for $\text{LiMg}_{0.10}\text{Co}_{0.90}\text{PO}_4$, $\text{LiMg}_{0.05}\text{Co}_{0.95}\text{PO}_4$ and LiCoPO_4 , respectively.

ARTICLE

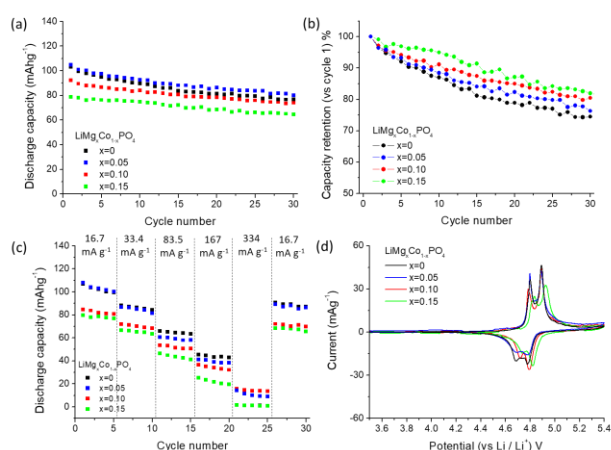


Fig. 7. (a) Galvanostatic cycling performance at a rate of 16.7 mA g^{-1} cycled between 3.5 and 5.0 V vs Li/Li^+ , (b) Normalised capacity retention based on the first cycle capacity, (c) Discharge capacity vs different current rates cycled between 3.5 and 5.0 V vs Li/Li^+ and (d) Voltammograms collected at a scan rate of $10 \mu\text{V s}^{-1}$ with the voltage window of 3.5 - 5.4 V vs Li/Li^+ of LiCoPO_4 (black), $\text{LiMg}_{0.05}\text{Co}_{0.95}\text{PO}_4$ (blue), $\text{LiMg}_{0.10}\text{Co}_{0.90}\text{PO}_4$ (red) and $\text{LiMg}_{0.15}\text{Co}_{0.85}\text{PO}_4$ (green).

A series of five cycles at progressively increasing current rates from 16.7 mA g^{-1} ($C/10$ for LiCoPO_4) to 334 mA g^{-1} ($2C$ for LiCoPO_4) was carried out to examine rate capability of Mg-doped samples. As shown in Fig. 7.c, at the lowest rate (16.7 mA g^{-1}) no significant effects are observed, whereas $\text{LiMg}_{0.05}\text{Co}_{0.95}\text{PO}_4$ and $\text{LiMg}_{0.10}\text{Co}_{0.90}\text{PO}_4$ demonstrate slightly better capacity compared to LiCoPO_4 at the highest rate (334 mA g^{-1}). This beneficial effect can be accounted for by the reduced anti-site defects as observed in the combined refinement results, which facilitates Li ion migration in the olivine structure. In the case of $\text{LiMg}_{0.15}\text{Co}_{0.85}\text{PO}_4$, the decrease in anti-site defects is probably offset by larger particles. All samples recover their capacity at 16.7 mA g^{-1} after cycling at higher rates, indicating that materials are preserved without significant degradation.

Cyclic voltammograms for all samples were collected by applying an initial positive potential and subsequent negative potential with a scan rate of $10 \mu\text{V s}^{-1}$ within the voltage range of 3.5 - 5.4 V (Fig. 7.d). Consistent with the charge/discharge curves, two oxidation and reduction peaks exist for all samples. Interestingly, the voltage of the two $\text{Co}^{2+}/\text{Co}^{3+}$ redox couples shift slightly to higher voltage with increasing Mg content from 4.73 and 4.82 V for LiCoPO_4 to 4.77 and 4.87 V for $\text{LiMg}_{0.15}\text{Co}_{0.85}\text{PO}_4$. The shift in redox potential has previously been observed in the phospho-olivine family e.g. $\text{LiMg}_x\text{Fe}_{1-x}\text{PO}_4$, $\text{LiMg}_x\text{Mn}_{1-x}\text{PO}_4$ and $\text{LiMg}_x\text{Co}_{1-x}\text{PO}_4$.^[14,46] As proposed in the other olivine systems, Mg^{2+} may stabilise the redox active $\text{Co}^{2+}/\text{Co}^{3+}$ through the TM^{2+} -O- Mg^{2+} interaction.

Origin of enhanced cycle stability

In order to gain better understanding of the enhanced cycle stability for Mg-doped LiCoPO_4 , *operando* XRD was carried out. This is a powerful technique to evaluate structural changes during cycling and is essential to investigate the delithiated phase ($\text{Mg}_x\text{Co}_{1-x}\text{PO}_4$) without its amorphisation which has often been observed for *ex-situ* measurements.^[57] The contour profile maps

of the XRD patterns for LiCoPO_4 and $\text{LiMg}_{0.15}\text{Co}_{0.85}\text{PO}_4$ in an *in-situ* cell cycled at a rate of 5.56 mA g^{-1} ($C/30$ for LiCoPO_4) during the charge process are shown in Fig. 8.a and in Fig. 8.b, respectively. The 2θ range 29 to 32° ($\text{Cu K}\alpha$, $\lambda = 1.5418 \text{ \AA}$) shows the (211) and the (020) reflections, which clearly reveals the changes in unit cell parameters upon cycling. For both samples two two-phase reactions, from the lithiated phase ($\text{LiMg}_x\text{Co}_{1-x}\text{PO}_4$, where $x=0$ and $x=0.15$) to the intermediate phase ($\text{Li}_{2/3}\text{Mg}_x\text{Co}_{1-x}\text{PO}_4$, where $x=0$ and $x=0.15$) and from the intermediate phase ($\text{Li}_{2/3}\text{Mg}_x\text{Co}_{1-x}\text{PO}_4$, where $x=0$ and $x=0.15$) to the delithiated phase ($\text{Mg}_x\text{Co}_{1-x}\text{PO}_4$, where $x=0$ and $x=0.15$), are observed through the simultaneous growth of reflections and loss of intensity of a new phase and an original phase, respectively.

Fig. 8.c shows the XRD patterns of LiCoPO_4 recorded during the first reaction ($\text{LiCoPO}_4 \rightarrow \text{Li}_{2/3}\text{CoPO}_4 + 1/3 \text{ Li}^+ + 1/3 \text{ e}^-$), there are the concurrent disappearance and appearance of the reflections of starting material and product, respectively, and shifts in the peak positions, implying solid-solution like behaviour as reported in previous studies.^[42,54,55] The peak shifts suggest that small structural changes in a limited range of two main compositions (LiCoPO_4 and $\text{Li}_{2/3}\text{CoPO}_4$) are required to nucleate a minority phase in a particle, reducing the energy between major and minor phases. An analogous phenomenon is observed for $\text{LiMg}_{0.15}\text{Co}_{0.85}\text{PO}_4$ as observed in Fig. 8.d, suggesting that the introduction of disorder in the olivine structure via Mg doping barely affects the appearance of the intermediate phase during the oxidation of Co^{2+} to Co^{3+} and the structural distortion to reduce the interphase energy. The following reaction ($\text{Li}_{2/3}\text{Mg}_x\text{Co}_{1-x}\text{PO}_4 \rightarrow \text{Mg}_x\text{Co}_{1-x}\text{PO}_4 + 1/3 \text{ Li}^+ + 1/3 \text{ e}^-$, where $x=0$ and $x=0.15$) similarly demonstrates two distinct phases with solid-solution like evolution (Fig. 8.e-f).

Rietveld refinements were carried out using the diffraction patterns acquired during the charge process. Due to the low resolution and different background, each pattern was independently refined. Atomic occupancies were fixed based on the ICP-OES values, whilst lattice parameters were refined to evaluate the unit cell volumes of each phase. Consistent with the shifts in peak positions, the volumes of all phases decrease along with the Li ion removal. Of note, the volume of the intermediate phase for both samples varies noticeably across the region where two phases coexist, implying that the intermediate phase sustains a larger solid solution region compared to the two end members. The intermediate phase is present until the end of charge, most likely due to the slow kinetics. The two major plateaus observed in the galvanostatic charge curve agree with the two-phase reaction regions with a slight lag probably due to the acquisition of each XRD pattern in a non-equilibrium state. It is worth noting that a plateau around 5.0 V in $\text{LiMg}_{0.15}\text{Co}_{0.85}\text{PO}_4$ can be attributed to side reactions whilst no important structural variation is shown (Fig. 8.f).

ARTICLE

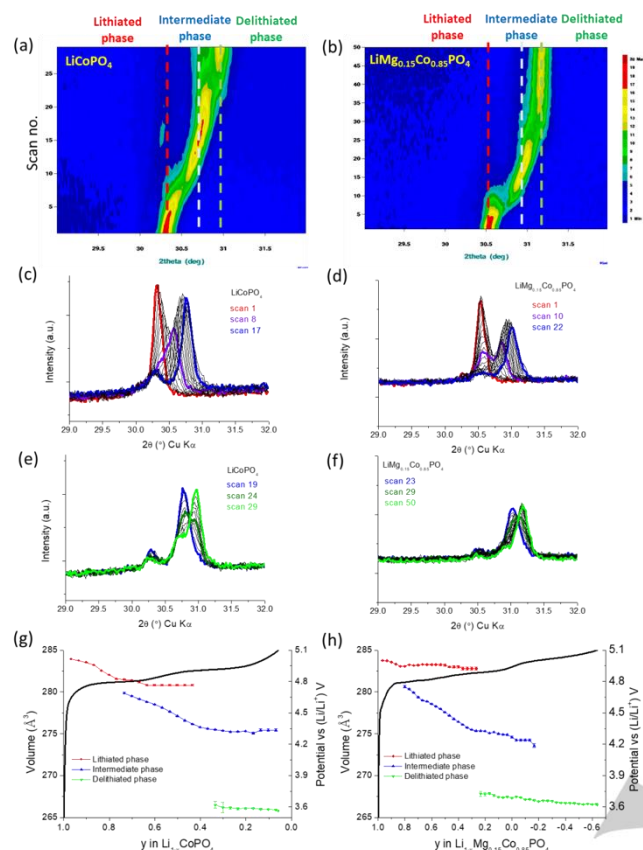


Fig. 8. The contour profile maps of the XRD patterns for the first charge of (a) LiCoPO_4 and (b) $\text{LiMg}_{0.15}\text{Co}_{0.85}\text{PO}_4$ cycled at a rate of 5.56 mA g^{-1} . The y-axis is scan number and x-axis is 2θ . The region $2\theta = 29$ to 32° shows the (211) and the (020) reflections. The red, light blue and green dotted vertical lines indicate the peak position of lithiated phase, intermediate phase and delithiated phase, respectively. XRD patterns of the phase transition from $\text{LiMg}_x\text{Co}_{1-x}\text{PO}_4$ to $\text{Li}_{2/3}\text{Mg}_x\text{Co}_{1-x}\text{PO}_4$ for (c) $x=0$ (i.e. scan numbers 1-17 with scan 8 in violet and scan 17 in blue) and (d) $x=0.15$ (i.e. scan numbers 1-22 with scan 1 in red, scan 10 in violet and scan 22 in blue). XRD patterns of the phase transition from $\text{Li}_{2/3}\text{Mg}_x\text{Co}_{1-x}\text{PO}_4$ to $\text{Mg}_x\text{Co}_{1-x}\text{PO}_4$ for (e) $x=0$ (i.e. scan numbers 19-29 with scan 19 in blue, scan 24 in olive and scan 29 in green) and (f) $x=0.15$ (i.e. scan numbers 23-50 with scan 23 in blue, scan 29 in olive and scan 50 in green). The Rietveld refinement results showing changes in the unit cell volumes in the three phases ($\text{LiMg}_x\text{Co}_{1-x}\text{PO}_4$ in red $\text{Li}_{2/3}\text{Mg}_x\text{Co}_{1-x}\text{PO}_4$ in blue $\text{Mg}_x\text{Co}_{1-x}\text{PO}_4$ in green) of (g) $x=0$ and (h) $x=0.15$, overlaid onto the galvanostatic charge curve cycled between 3.5 and 5.1 V vs Li/Li^+ at 5.56 mA g^{-1} .

The volume change between lithiated and delithiated phase was examined using the Le Bail refinement of the two end XRD patterns acquired from *operando* XRD measurements (Fig. 9). The variation of unit cell volume between the pristine and the end of charge phase varies from 6.52 % for LiCoPO_4 to 6.15 % $\text{LiMg}_{0.15}\text{Co}_{0.85}\text{PO}_4$. Lower volume variation is found along with the increase in Mg content since electrochemically inactive Mg^{2+} ions reside within the structure during cycling. Reducing the lattice stress caused by the unit cell volume mismatch during electrochemical cycling might be a source of improved cyclability of $\text{LiMg}_{0.15}\text{Co}_{0.85}\text{PO}_4$ at the expense of initial capacity.

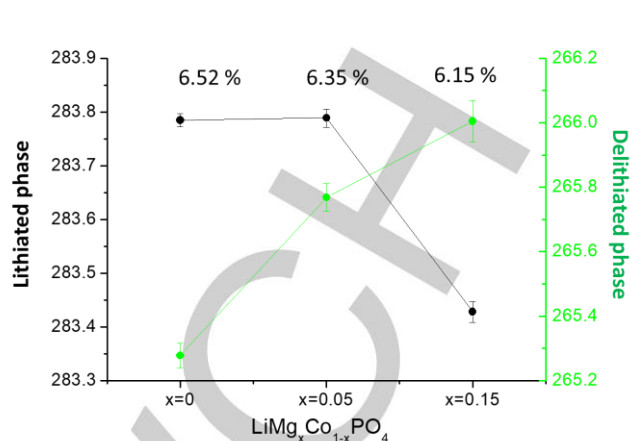


Fig. 9. Variation of unit cell volume between lithiated and delithiated phase for LiCoPO_4 , $\text{LiMg}_{0.05}\text{Co}_{0.95}\text{PO}_4$ and $\text{LiMg}_{0.15}\text{Co}_{0.85}\text{PO}_4$.

In addition to the structural stabilisation, the Mg-rich layer present in $\text{LiMg}_{0.15}\text{Co}_{0.85}\text{PO}_4$ particles may play a critical role in enhancing cycling stability. One of the reasons for capacity fade of LiCoPO_4 is interfacial reactions between active materials and the electrolyte, i.e. nucleophilic attack of F^- produced in LiPF_6 based electrolyte causes degradation of active materials through the breakage of phosphate groups.^[58,59] One potential method to alleviate the undesired reactions is modifying the surface of the active materials with thin metal oxides such as NiO ,^[60] VO_x ,^[20] or Al_2O_3 .^[61] In various studies of LiCoO_2 , MgO coating has been revealed as an effective way to improve cycling ability.^[62-64] Assuming that the Mg-rich layer observed on the surface of as-synthesised $\text{LiMg}_{0.15}\text{Co}_{0.85}\text{PO}_4$ can act as a protective layer, inhibiting direct contact between bulk active material and the electrolyte, the surface of $\text{LiMg}_{0.15}\text{Co}_{0.85}\text{PO}_4$ after the first cycle was analysed. As shown in Fig. 10, the Mg-rich layer (about 15 nm) remains after cycling without significant amorphisation of active material, supporting the protective role of Mg-rich layer.

ARTICLE

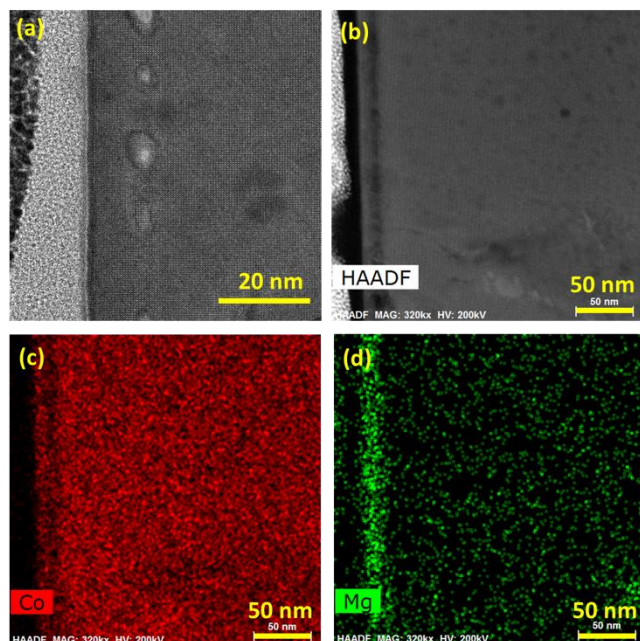


Fig. 10. (a) Bright-field TEM image, (b) High-angle annular dark-field STEM image and EDS mapping for (c) Co and (d) Mg elements of post-cycled $\text{LiMg}_{0.15}\text{Co}_{0.85}\text{PO}_4$.

Unlike carbon coating which provides enhanced overall electronic conductivity of electrodes, metal oxide coating on the surface of active material might impede Li ion diffusion and increase resistance of the electrodes.^[20,62] To evaluate the influence of the Mg-rich layer on the resistance of $\text{LiMg}_{0.15}\text{Co}_{0.85}\text{PO}_4$ electrodes, electrochemical impedance spectroscopy (EIS) measurements were carried out. Fig. 11 shows the Nyquist plots of LiCoPO_4 and $\text{LiMg}_{0.15}\text{Co}_{0.85}\text{PO}_4$ electrodes before and after cycling. As-assembled LiCoPO_4 and $\text{LiMg}_{0.15}\text{Co}_{0.85}\text{PO}_4$ electrodes display an arc followed by an angled line whereas their post-cycled electrodes exhibit an extra arc before the angled line.

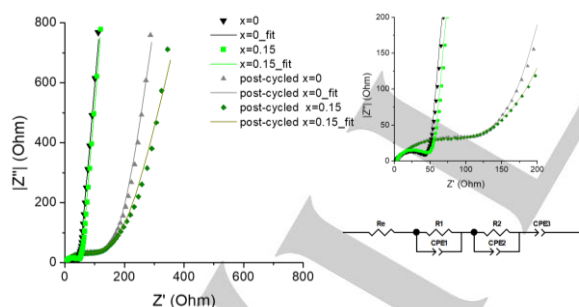


Fig. 11. Nyquist plots of as-assembled and post-cycled LiCoPO_4 and $\text{LiMg}_{0.15}\text{Co}_{0.85}\text{PO}_4$ electrodes at frequencies from 0.1 Hz to 0.1 MHz, with a zoomed image for high frequency on the top right and an equivalent circuit on the bottom right.

The size of the arcs is comparable between LiCoPO_4 and $\text{LiMg}_{0.15}\text{Co}_{0.85}\text{PO}_4$ electrodes in both stages, as-assembled and after cycling, implying that the Mg-rich layer barely affects electrode resistance. Fitting results (Table S2) using an equivalent circuit reveal that similar processes occur in as-assembled LiCoPO_4 and $\text{LiMg}_{0.15}\text{Co}_{0.85}\text{PO}_4$ electrodes with resistances of 44.3 and 47.5 Ω , respectively, which can be

associated with the resistance of the active material/electrolyte interface and charge transfer within the electrodes as well as active material particles. It is noted that R2 was included to fit post-cycled LiCoPO_4 and $\text{LiMg}_{0.15}\text{Co}_{0.85}\text{PO}_4$ electrodes due to the appearance of an additional arc which could represent SEI layer resistance.

Conclusions

Magnesium doped lithium cobalt phosphates, $\text{LiMg}_x\text{Co}_{1-x}\text{PO}_4$ ($x = 0, 0.05, 0.10, 0.15$ and 0.20), were synthesised using a solvothermal method. It is shown that 15 % substitution of Mg for Co is the limit to obtain a single-phase which crystallises in the olivine structure. Structural investigation using XRD data and elemental analysis using ICP-OES and EDS provide evidence of successful Mg doping in Co sites. Detailed crystallographic information was obtained using combined Rietveld refinement, revealing that preferential occupation of Mg in Co sites reduces anti-site defects. In terms of morphology, the increase in Mg content tends to enlarge particle size, leading to noticeably large particles in $\text{LiMg}_{0.15}\text{Co}_{0.85}\text{PO}_4$.

Given these effects driven by Mg doping, electrochemical performance of $\text{LiMg}_x\text{Co}_{1-x}\text{PO}_4$ ($x = 0, 0.05, 0.10$ and 0.15) was examined. The two biphasic redox mechanism is maintained for all samples with a slight upward shift in working voltage for $\text{LiMg}_{0.15}\text{Co}_{0.85}\text{PO}_4$. Regarding cycling stability, Mg-doped LiCoPO_4 samples demonstrate better capacity retention. Enhancement in rate capability is observed for $\text{LiMg}_{0.10}\text{Co}_{0.90}\text{PO}_4$ possibly due to reduction of anti-site defects without enlargement of particle size, which favours Li ion migration.

Operando XRD and *ex-situ* TEM measurements shed light on the improved cycling performance of $\text{LiMg}_{0.15}\text{Co}_{0.85}\text{PO}_4$. From a structural point of view, smaller volume changes between lithiated and delithiated phase mitigates lattice stress, leading to the maintenance of the initial capacity upon cycling. A Mg-rich layer present on the surface of particles can act as a protective layer preventing detrimental reactions between the active material and the electrolyte.

In conclusion, Mg substitution for Co in LiCoPO_4 may be one of the strategies to alleviate capacity fade via structural stabilisation during cycling and surface protection preventing a direct contact with the electrolyte.

Experimental Section

Synthesis of $\text{LiMg}_x\text{Co}_{1-x}\text{PO}_4$ ($x = 0, 0.05, 0.10, 0.15$ and 0.20) Samples were synthesised by a solvothermal method previously reported by Brutti and co-workers with slight modification.^[7,47] Two aqueous solutions: solution A with lithium hydroxide monohydrate ($\text{LiOH}\cdot\text{H}_2\text{O}$, Sigma-Aldrich, $\geq 98\%$) and solution B containing lithium dihydrogen phosphate (LiH_2PO_4 , Alfa Aesar, 97%), cobalt sulphate heptahydrate ($\text{CoSO}_4\cdot 7\text{H}_2\text{O}$, Sigma-Aldrich, $\geq 99\%$), and D-(+)-glucose (Sigma-Aldrich) were prepared separately. The solution A was added to ethylene glycol to give solution C. Subsequently the solution B was added dropwise into the solution C under stirring. The molar ratio of $\text{LiOH}\cdot\text{H}_2\text{O} : \text{CoSO}_4\cdot 7\text{H}_2\text{O} : \text{LiH}_2\text{PO}_4 : \text{D-(+)-glucose}$ was 1.75 : 1 : 1 : 0.03. The Co^{2+} concentration in the final ethylene

ARTICLE

glycol/water solution was 0.1 M. The obtained purple suspension was sealed in a 45 ml Teflon-lined autoclave and heated in an oven at 220 °C for 16 h. The product was filtered, washed with water and ethanol then dried at 80 °C. A series of magnesium substituted LiCoPO_4 , $\text{LiMg}_x\text{Co}_{1-x}\text{PO}_4$ ($x = 0.05, 0.10, 0.15$ and 0.20), was obtained by using an additional reagent magnesium sulphate (MgSO_4 , Sigma-Aldrich, $\geq 99.5\%$) and setting the relative molar ration of $\text{CoSO}_4 \cdot 7\text{H}_2\text{O}$ and MgSO_4 to the desired ratio in the solution B.

Analyses and characterisation of magnesium doped lithium cobalt phosphate materials Powder X-ray diffraction (PXRD) patterns were collected on a STOE STADI/P diffractometer operating in transmission mode with $\text{Fe K}\alpha_1$ radiation ($\lambda = 1.936 \text{ \AA}$). Lattice parameters were obtained by the Le Bail method using the GSAS package with the EXPGUI interface.^[65] For combined refinements, the pattern for $\text{LiMg}_{0.15}\text{Co}_{0.85}\text{PO}_4$ was collected on a PANalytical Empyrean diffractometer in Bragg-Brentano geometry with $\text{Cu K}\alpha_1$ radiation ($\lambda = 1.5406 \text{ \AA}$). Time-of-flight powder neutron diffraction (PND) data were obtained on the Polaris diffractometer at ISIS at the Rutherford Appleton Laboratory. Samples were contained in 6 mm vanadium cans. Detailed crystallographic information was obtained from combined refinements using powder neutron and X-ray diffraction data. Rietveld refinements were carried out using the program Topas Academic.^[66] Inductively coupled plasma optical emission spectroscopy (ICP-OES) analysis was performed using a iCAP 6000 Series. Transmission electron microscopy (TEM) and scanning transmission electron microscope (STEM) images were taken by using a FEI Titan Themis 200 and Energy dispersive X-ray spectroscopy (EDS) mapping was collected with a Super-X high sensitivity windowless EDX detector. EDS spectra were collected at an acceleration voltage of 15 keV using a FEI Scios microscope equipped with EDAX Octane Plus EDS detector. Scanning electron microscopy (SEM) images were recorded on a JEOL JSM-6700F.

Electrochemical characterisation To evaluate electrochemical performance of materials, slurries were prepared using the active material, super C65 carbon and Solef 5130 binder (a modified polyvinylidene fluoride (PVDF)) in the mass ratio 75: 15: 10 in *n*-methyl-2-pyrrolidone, which was then cast on aluminium foil using a doctor blade. After drying, electrode sheets were calendared and 13 mm diameter electrode discs were punched then dried at 80 °C under vacuum for 12 h. For *operando* XRD measurement and *ex-situ* TEM analysis, working electrodes were constructed by mixing the active material and super C65 carbon in the mass ratio 71: 29. The mixture was dried at 110 °C under vacuum for 12 h. LIR2032 coin cells were assembled in an Ar-filled glovebox and used for evaluation of electrochemical performance except electrochemical impedance spectroscopy (EIS) measurements where CR2325 coin cells were assembled. The cells consisted of a disc electrode, lithium metal as a counter/reference electrode, a glass fibre separator (Whatman, GF/B) and LP30 electrolyte (1M LiPF_6 in ethylene carbonate : dimethyl carbonate = 1:1 w/w). For *ex-situ* TEM measurement, Swagelok-type cells were assembled in an Ar-filled glovebox. The cells consisted of a desired amount of working electrode, consisted of 71 wt % active material and 29 wt % super C65 with no binder, lithium metal as a counter/reference electrode, glass fibre separators (Whatman, GF/B) and LP30 electrolyte (1M LiPF_6 in ethylene carbonate : dimethyl carbonate = 1:1 w/w). Galvanostatic charge/discharge cycling and voltage scans (linear sweep voltammetry) were carried out using a Bio-logic VMP 3. EIS measurements were conducted on CR2325 coin cells, cycled at 30 °C using a Maccor Series 4200 battery cycler. Data for pre- and post-cycled cells were collected using a Solartron 1255 frequency response analyser coupled with Solartron 1287 electrochemical interface. A perturbation voltage of 10 mV and frequency range from 0.1 Hz to 0.1 MHz were employed.

Operando XRD measurements *Operando* XRD patterns were recorded on a D8 Advance Bruker diffractometer using $\text{Cu K}\alpha$ radiation ($\lambda = 1.5418 \text{ \AA}$) in the 2θ range $10^\circ - 44^\circ$ with a scan step width of 0.0197° and a scan rate of 1.8 s per step, corresponding to an hour of electrochemical reaction per pattern. For the *operando* XRD measurements the in-house *in-situ* cell^[67] equipped with a beryllium window was used with a thin aluminum foil (Goodfellow, 99.1 %) to prevent the window from possible oxidation at high voltage. Rietveld refinement was carried out using the Fullprof suite.^[68]

Ex-situ TEM measurement For *ex-situ* TEM measurement, cycled cells were transferred to an Ar-filled glovebox before opening and the active material was extracted. The electrodes were rinsed carefully with dry dimethyl carbonate to remove residual electrolyte and then left under vacuum to ensure all solvent had evaporated. To minimise moisture/air exposure to the sample, the extracted active material was loaded in a sample holder inside the glovebox and quickly transferred to a FEI Scios microscope for milling the sample, then kept under vacuum until TEM measurement, which was carried out as described for as-synthesised samples.

Acknowledgements

EJK would like to thank the Alistore ERI for the award of a studentship, ScotChem for an award of postgraduate and early career researcher exchanges (PECRE) and Christian Masquelier for his supervision at LRCS. The authors thank EPSRC Capital for Great Technologies Grant EP/L017008/1 and are grateful for the provision of beam time and assistance from instrument scientist at Polaris diffractometer at ISIS at the Rutherford Appleton Laboratory.

Keywords: Lithium cobalt phosphate • Lithium ion battery • Magnesium doping • High voltage positive electrode materials • Operando X-ray diffraction

- [1] K. Amine, H. Yasuda, M. Yamachi, *Electrochem. Solid-State Lett.* **2000**, *3*, 178–179.
- [2] J. Wolfenstine, *J. Power Sources* **2006**, *158*, 1431–1435.
- [3] J. L. Allen, T. Thompson, J. Sakamoto, C. R. Becker, T. R. Jow, J. Wolfenstine, *J. Power Sources* **2014**, *254*, 204–208.
- [4] M. E. Rabanal, M. C. Gutierrez, F. Garcia-Alvarado, E. C. Gonzalo, M. E. Arroyo-de Dompablo, *J. Power Sources* **2006**, *160*, 523–528.
- [5] M. Prabu, S. Selvasekarapandian, A. R. Kulkarni, S. Karthikeyan, G. Hirankumar, C. Sanjeeviraja, *Solid State Sci.* **2011**, *13*, 1714–1718.
- [6] N. N. Bramnik, K. G. Bramnik, T. Buhrmester, C. Baehtz, H. Ehrenberg, H. Fuess, *J. Solid State Electrochem.* **2004**, *8*, 558–564.
- [7] S. Brutti, J. Manzi, A. De Bonis, D. Di Lecce, F. Vitucci, A. Paolone, F. Trequattrini, S. Panero, *Mater. Lett.* **2015**, *145*, 324–327.
- [8] N. N. Bramnik, D. M. Trots, H. J. Hofmann, H. Ehrenberg, *Phys. Chem. Chem. Phys.* **2009**, *11*, 3271–3277.
- [9] Y.-M. Kang, Y.-I. Kim, M.-W. Oh, R.-Z. Yin, Y. Lee, D.-W. Han, H.-S. Kwon, J. H. Kim, G. Ramanath, *Energy Environ. Sci.* **2011**, *4*, 4978–4983.
- [10] N. V. Kosova, O. A. Podgornova, E. T. Devyatkina, V. R. Podgolinikov, S. A. Petrov, *J. Mater. Chem. A* **2014**, *2*, 20697–20705.
- [11] S. Brutti, J. Manzi, D. Meggiolaro, F. M. Vitucci, F. Trequattrini, A. Paolone, O. Palumbo, *J. Mater. Chem. A* **2017**, *5*, 14020–14030.
- [12] H. Li, Y. Wang, X. Yang, L. Liu, L. Chen, J. Wei, *Solid State Ionics* **2014**, *255*, 84–88.
- [13] L. Dimesso, C. Spanheimer, W. Jaegermann, *J. Power Sources* **2013**, *243*, 668–675.
- [14] L. Dimesso, C. Spanheimer, W. Jaegermann, *J. Alloys. Compd.*

ARTICLE

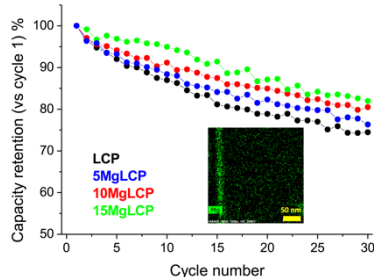
- [15] 2014, 582, 69–74.
L. Dimesso, D. Becker, C. Spanheimer, W. Jaegermann, *Prog. Solid State Chem.* **2014**, *42*, 184–190.
- [16] M. V. V. M. S. Kishore, U. V. Varadaraju, *Mater. Res. Bull.* **2005**, *40*, 1705–1712.
- [17] Y. Maeyoshi, S. Miyamoto, Y. Noda, H. Munakata, K. Kanamura, *J. Power Sources* **2017**, *337*, 92–99.
- [18] A. Örnek, M. Can, A. Yeşildağ, *Mater. Charact.* **2016**, *116*, 76–83.
- [19] B. Wu, H. Xu, D. Mu, L. Shi, B. Jiang, L. Gai, L. Wang, Q. Liu, L. Ben, F. Wu, *J. Power Sources* **2016**, *304*, 181–188.
- [20] N. Laszczynski, A. Birrozzi, K. Maranski, M. Copley, M. E. Schuster, S. Passerini, *J. Mater. Chem. A* **2016**, *4*, 17121–17128.
- [21] J. Ni, L. Gao, L. Lu, *J. Power Sources* **2013**, *221*, 35–41.
- [22] X.-K. Ding, L.-L. Zhang, X.-L. Yang, H. Fang, Y.-X. Zhou, J.-Q. Wang, D. Ma, *ACS Appl. Mater. Interfaces* **2017**, *9*, 42788–42796.
- [23] L.-L. Zhang, G. Liang, G. Peng, Y.-H. Huang, L. Wang, L. Qie, M. C. Croft, A. Ignatov, J. B. Goodenough, *J. Electrochem. Soc.* **2012**, *159*, A1573–A1578.
- [24] X. Rui, X. Zhao, Z. Lu, H. Tan, D. Sim, H. H. Hng, R. Yazami, T. M. Lim, Q. Yan, *ACS Nano* **2013**, *7*, 5637–5646.
- [25] M. K. Devaraju, D. Rangappa, I. Honma, *Electrochim. Acta* **2012**, *85*, 548–553.
- [26] J. Liu, T. E. Conry, X. Song, L. Yang, M. M. Doeff, T. J. Richardson, *J. Mater. Chem.* **2011**, *21*, 9984–9987.
- [27] L.-L. Zhang, Z. Li, X.-L. Yang, X.-K. Ding, Y.-X. Zhou, H.-B. Sun, H.-C. Tao, L.-Y. Xiong, Y.-H. Huang, *Nano Energy* **2017**, *34*, 111–119.
- [28] R. Sharabi, E. Markevich, V. Borgel, G. Salitra, D. Aurbach, G. Semrau, M. A. Schmidt, N. Schall, C. Stinner, *Electrochem. Commun.* **2011**, *13*, 800–802.
- [29] Y. Maeyoshi, S. Miyamoto, H. Munakata, K. Kanamura, *J. Power Sources* **2017**, *350*, 103–108.
- [30] R. Sharabi, E. Markevich, K. Fridman, G. Gershinsky, G. Gershinsky, G. Salitra, G. Semrau, D. Aurbach, N. Schall, M. A. Schmidt, N. Schall, C. Bruenig, *Electrochem. Commun.* **2013**, *28*, 20–23.
- [31] L. Y. Xing, M. Hu, Q. Tang, J. P. Wei, X. Qin, Z. Zhou, *Electrochim. Acta* **2012**, *59*, 172–178.
- [32] T. Fukutsuka, T. Nakagawa, K. Miyazaki, T. Abe, *J. Power Sources* **2016**, *306*, 753–757.
- [33] E. J. Kim, X. Yue, J. T. S. Irvine, A. R. Armstrong, *J. Power Sources* **2018**, *403*, 11–19.
- [34] J. Wang, X. Sun, *Energy Environ. Sci.* **2015**, *8*, 1110–1138.
- [35] K. J. Kreder, G. Assat, A. Manthiram, *Chem. Mater.* **2016**, *28*, 1847–1853.
- [36] F. Wang, J. Yang, Y. NuLi, J. Wang, *J. Power Sources* **2010**, *195*, 6884–6887.
- [37] J. L. Allen, T. R. Jow, J. Wolfenstine, *J. Power Sources* **2011**, *196*, 8656–8661.
- [38] J. L. Allen, J. L. Allen, T. Thompson, S. A. Delp, J. Wolfenstine, T. R. Jow, *J. Power Sources* **2016**, *327*, 229–234.
- [39] F. C. Strobridge, D. S. Middlemiss, A. J. Pell, M. Leskes, R. J. Clément, F. Pourpoint, Z. Lu, J. V. Hanna, G. Pintacuda, L. Emsley, A. Samoson, C. P. Grey, *J. Mater. Chem. A* **2014**, *2*, 11948–11957.
- [40] D. Di Lecce, J. Manzi, F. M. Vitucci, A. De Bonis, S. Panero, S. Brutti, *Electrochim. Acta* **2015**, *185*, 17–27.
- [41] L. Fang, H. Zhang, Y. Zhang, L. Liu, Y. Wang, *J. Power Sources* **2016**, *312*, 101–108.
- [42] F. C. Strobridge, H. Liu, M. Leskes, O. J. Borkiewicz, K. M. Wiaderek, P. J. Chupas, K. W. Chapman, C. P. Grey, *Chem. Mater.* **2016**, *28*, 3676–3690.
- [43] V. Ramar, P. Balaya, *Phys. Chem. Chem. Phys.* **2013**, *15*, 17240.
- [44] M. Memm, M. Koentje, P. Axmann, M. Wohlfahrt-Mehrens, *J. Power Sources* **2015**, *276*, 382–387.
- [45] M. Köntje, M. Memm, P. Axmann, M. Wohlfahrt-Mehrens, *Prog. Solid State Chem.* **2014**, *42*, 106–117.
- [46] T. Muraliganth, A. Manthiram, *J. Phys. Chem. C* **2010**, *114*, 15530–15540.
- [47] J. Manzi, M. Curcio, S. Brutti, *Nanomaterials* **2015**, *5*, 2212–2230.
- [48] D. Y. W. Yu, K. Donoue, T. Kadohata, T. Murata, S. Matsuta, S. Fujitani, *J. Electrochem. Soc.* **2008**, *155*, A526–A530.
- [49] C. A. J. Fisher, V. M. H. Prieto, M. S. Islam, *Chem. Mater.* **2008**, *20*, 5907–5915.
- [50] J. Ludwig, J. Ludwig, C. Marino, C. Marino, D. Haering, C. Stinner, D. Haering, D. Nordlund, C. Stinner, D. Nordlund, M. N. Doeff, H. A. Gasteiger, T. Nilges, *RSC Adv.* **2016**, *6*, 82984–82994.
- [51] J. Ludwig, C. Marino, D. Haering, C. Stinner, H. A. Gasteiger, T. Nilges, *J. Power Sources* **2017**, *342*, 214–223.
- [52] X. Qin, X. Wang, H. Xiang, J. Xie, J. Li, Y. Zhou, *J. Phys. Chem. C* **2010**, *114*, 16806–16812.
- [53] M. G. Palmer, J. T. Frith, A. L. Hector, A. W. Lodge, J. R. Owen, C. Nicklin, J. Rawle, *Chem. Commun.* **2016**, *52*, 14169–14172.
- [54] F. C. Strobridge, R. J. Clément, M. Leskes, D. S. Middlemiss, O. J. Borkiewicz, K. M. Wiaderek, K. W. Chapman, P. J. Chupas, C. P. Grey, *Chem. Mater.* **2014**, *26*, 6193–6205.
- [55] M. Kaus, I. Issac, R. Heinzmann, S. Doyle, S. Mangold, H. Hahn, V. S. K. Chakravadhanula, C. Kübel, H. Ehrenberg, S. Indris, *J. Phys. Chem. C* **2014**, *118*, 17279–17290.
- [56] J. Billaud, G. Singh, A. R. Armstrong, E. Gonzalo, V. Roddatis, M. Armand, T. Rojo, P. G. Bruce, *Energy Environ. Sci.* **2014**, *7*, 1387–1391.
- [57] N. N. Bramnik, K. G. Bramnik, C. Baetz, H. Ehrenberg, *J. Power Sources* **2005**, *145*, 74–81.
- [58] R. Sharabi, E. Markevich, V. Borgel, G. Salitra, G. Gershinsky, D. Aurbach, G. Semrau, M. A. Schmidt, N. Schall, C. Stinner, *J. Power Sources* **2012**, *203*, 109–114.
- [59] E. Markevich, R. Sharabi, H. Gottlieb, V. Borgel, K. Fridman, G. Salitra, D. Aurbach, G. Semrau, M. A. Schmidt, N. Schall, C. Bruenig, *Electrochem. Commun.* **2012**, *15*, 22–25.
- [60] A. Örnek, *Journal of Power Sources* **2017**, *356*, 1–11.
- [61] A. Eftekhari, *J. Electrochem. Soc.* **2004**, *151*, A1456–A1460.
- [62] H. Zhao, L. Gao, W. Qiu, X. Zhang, *J. Power Sources* **2004**, *132*, 195–200.
- [63] Y. Orikasa, D. Takamatsu, K. Yamamoto, Y. Koyama, S. Mori, T. Masese, T. Mori, T. Minato, H. Tanida, T. Uruga, Z. Ogumi, Y. Uchimoto, *Adv. Mater. Interfaces* **2014**, *1*, 1400195–1400202.
- [64] J.-H. Shim, S. Lee, S. S. Park, *Chem. Mater.* **2014**, *26*, 2537–2543.
- [65] B. H. Toby, *J. Appl. Crystallogr.* **2001**, *34*, 210–213.
- [66] A. A. Coelho, *J. Appl. Crystallogr.* **2000**, *33*, 899–908.
- [67] M. Morcrette, J. B. Leriche, S. Patoux, C. WURM, C. Masquelier, *Electrochem. Solid-State Lett.* **2003**, *6*, A80–A84.
- [68] J. Rodríguez-Carvajal, *Phys. B* **1993**, *192*, 55–69.

ARTICLE

Entry for the Table of Contents (Please choose one layout)

ARTICLE

Cycling stability of LiCoPO_4 as a high voltage positive electrode material in lithium ion batteries is enhanced by partial Mg substitution for Co. The combined benefits of the decrease in anti-site defects, the reduced lattice stress during electrochemical cycling and the Mg-rich layer on the surface result in improved capacity retention in Mg-doped LiCoPO_4 .



Eun Jeong Kim, David Miller, John T.S. Irvine and A. Robert Armstrong*

Page No. – Page No.

Enhanced cycling performance of magnesium doped lithium cobalt phosphate